

Fast inflowing ionized absorber tracing the gas dynamics at sub-parsec scale around Mrk 3

FANGZHENG SHI (施方正) ¹, MATTEO GUAINAZZI,² AND YIJUN WANG (王倚君)^{3,4}

¹*Shanghai Astronomical Observatory, Chinese Academy of Science, No.80 Nandan Road, Shanghai, China*

²*European Space Agency (ESA), European Space Research and Technology Centre (ESTEC), Noordwijk, The Netherlands*

³*School of Astronomy and Space Science, Nanjing University, 163 Xianlin Avenue, Nanjing 210023, People' s Republic of China*

⁴*Key Laboratory of Modern Astronomy and Astrophysics, Nanjing University, Ministry of Education, 163 Xianlin Avenue, Nanjing 210023, People' s Republic of China*

ABSTRACT

Accretion onto supermassive black hole (SMBH) releases energy via radiation, jets or winds, providing feedback effects on the circumnuclear gas environment. However, the dynamics of accreting gas on sub-parsec scales near the SMBH remains poorly understood. With high-resolution X-ray spectra of Mrk 3, we detect a fast inflowing ionized absorber characterized by redshifted Fe XXV and Fe XXVI absorption lines. Photoionization modeling reveals the inflowing absorber is located at $\lesssim 0.04 - 0.74$ pc and is decelerating from $6.1 \pm 0.5 \times 10^3$ km s⁻¹ to $3.4 \pm 0.3 \times 10^3$ km s⁻¹ over 11 years. Only $\sim 0.6\% - 3\%$ of the inflowing material is estimated to reach the event horizon. This direct evidence of sub-parsec scale fueling inflow bridges the gap between the torus and the outer accretion disk. Furthermore, a 0.86-keV gas component with sub-solar metallicity ($Z \sim 0.22$), outflowing at a velocity of ~ 330 km s⁻¹, is detected in the soft X-ray band. It may corresponds to the [O III] biconical outflow in the narrow-line region. A putative ultra-fast disk wind outside our line-of-sight, or clouds within the broad-line region, are promising candidates for decelerating the inflowing absorber.

Keywords: High energy astrophysics (739) — Accretion(14) — X-ray active galactic nuclei(2035) — Photoionization(2060)

1. INTRODUCTION

A supermassive black hole (SMBH) at the center of nearly every galaxy has been considered as an essential component to galaxy evolution. Actively accreting SMBHs, manifesting themselves as active galactic nuclei (AGN) can convert accretion power into considerable energy output in the form of radiation, jets or winds, thereby regulating both black hole growth and star formation—an effect known as AGN feedback (Fabian 2012). The infalling motion of cold accretion gas toward the central SMBH can be traced from extragalactic scales (through galaxy mergers and interaction), galactic scales (through secular processes), down to sub-hundred-parsec scale (through nuclear gas disks, bars or spirals)(Storchi-Bergmann & Schnorr-Müller 2019). At smaller scales, Shi et al. (2016) detected a redshifted absorber in the spectra of a quasar and found that the

inflowing medium is located at ~ 4 pc from the black hole near the AGN torus with reverberation mapping.

However, observational evidence of cold gas inflow that directly feeds black hole accretion disks on sub-parsec scales remains limited. In a small sample of quasars around $z \sim 1$ (e.g. in J1035+1422), redshifted broad absorption lines reaching $\sim 1000 - 5000$ km s⁻¹ have been detected coexisting with blueshifted absorption lines. These observations features a potential feeding inflow, possibly connecting between the torus and the accretion disk within several $10^{3-4} r_g$, in addition to the disk wind(Zhou et al. 2019; Chen et al. 2022). Izumi et al. (2023) resolved a gravitationally unstable, dense gas disk driving sub-parsec scale accretion inflow onto the black hole in the Circinus Galaxy. Only 3% of the inflowing material is estimated to reach the event horizon, with the rest ejected by multiphase outflows.

Zhou et al. (2019) proposes the AGN torus as the gas reservoir fueling the accretion disk and attributes the scarcity of observed disk-feeding inflow to an observational bias due to line-of-sight effect. When the line of

sight is close to the polar direction, it intercepts only the blueshifted, disk driven outflow aligned with the narrow-line region (NLR). Conversely, when the line of sight inclining towards the torus plane, the inflow material would be totally obscured by the optically thick torus. Only a modest inclination angle grazing the surface of the dusty torus, would enable a direct detection piercing through the inflowing medium connecting to the accretion disk.

As gas approaches sub-parsec scale toward the central AGN, it becomes heavily photoionized by the intense radiation field. The physical properties of such highly ionized gas are best probed through X-ray spectroscopy. Highly ionized, ultra-fast outflows characterized by blueshifted UV / X-ray absorption lines are ubiquitously found in up to 30–50% of local AGN (Crenshaw & Kraemer 2012; Tombesi et al. 2010), while their redshifted counterparts, fast inflows at sub-parsec scales are rarely reported. Therefore, detailed X-ray spectroscopic studies of individual AGN observed at grazing angles in the local Universe would help reveal the complex ‘inflow-outflow’ gas dynamics in the very vicinity of AGN and the narrow-line region.

Lying at a distance of 58.5 Mpc ($z \sim 0.0135^1$), Mrk 3 (Markarian 3) is an $S0$ -type galaxy hosting a nearly obscured, Compton-thin AGN (Yaqoob et al. 2015). The mass of the central supermassive black hole is estimated to be $\log(M_{\text{BH}}) = 8.65$ based on stellar velocity dispersion (Woo & Urry 2002). The Eddington ratio of Mrk 3 ranges between 0.01 and 0.04. Signatures of ionized gas outflows have been discovered and well-studied in Mrk 3. Kinematic modeling of emission lines (e.g., [O III], [N II]) reveals a peak gas velocity of $\sim 500 - 1500 \text{ km s}^{-1}$ in the narrow-line region (NLR), tracing a biconical outflow extending to $\sim 400 \text{ pc}$ (Ruiz et al. 2001; Collins et al. 2005; Gnilka et al. 2020; Revalski et al. 2021; Meena et al. 2023). Diffuse X-ray emission observed in Chandra 0-order image reveals that the highly ionized gas extends along the direction roughly coincident with the [O III] outflow in the NLR (Bogdán et al. 2017). Guainazzi et al. (2016) analyzed the X-ray broadband spectrum of Mrk 3 with the state-of-the-art torus model to investigate its torus properties (including the torus opening angle). They concluded that the line-of-sight intercepts the torus surface. This makes Mrk 3 analogous to those $z \sim 1 - 2$ quasars with a torus-grazing viewing angle mentioned above. They also reported the detection of redshifted, highly-ionized iron absorption

lines in the stacked Chandra HEG spectrum, but left their origin unexplained.

Therefore, our motivation is to investigate the properties of the ionized absorber in detail, to explore the connection between torus, accretion inflows and outflows, and to get a better understanding of the hot gas dynamics and feedback effect in the vicinity of the central AGN in Mrk 3. This paper is organized as follows. In Section 2 we describe the data reduction processes in detail. In Section 3, results of spectral fitting for both soft and hard X-ray bands are presented, as well as a detailed photoionization modeling for potential redshifted ionized absorber. In Section 4, we try to propose a preferred scenario to explain the multi-scale, multi-phase dynamical behavior of the gas from sub-parsec to hundred parsec around Mrk 3 nuclei. We summarize our findings in Section 5.

2. DATA REDUCTION

To detect plasma with bulk motion around the Mrk 3 nucleus, all available high-resolution X-ray spectroscopic data covering both soft and hard X-ray bands has been retrieved. The High Energy Transmission Grating (HETG) onboard Chandra X-ray Observatory, covering the energy band ranging from 1 – 10 keV, can retain a spectral resolution of $\sim 2000 \text{ km s}^{-1}$ around the iron fluorescent lines (6 – 7.5 keV). For the soft X-ray band, the XMM-Newton Reflection Grating Spectrometer (RGS) offers a first-order full-width half maximum (FWHM) spectral resolution of $\sim 1200 \text{ km s}^{-1}$ over 0.5–2 keV range. We summarize the basic information of all the observations in Table 1.

2.1. HETG

Mrk 3 has been observed by HETG in 2000 and 2011 for a total clean exposure of 389.3 ks. We reduce the data with the CIAO v4.15 software package (Fruscione et al. 2006). The $\pm 1st$ -order High Energy Gratings (HEG) spectra have been extracted for all epochs. Half-width of the source extraction region in the cross-dispersion direction corresponds to $\lesssim 680 \text{ pc}$ in physical size for Mrk 3. The underlying continuum shows little variability, so all spectra are co-added for a baseline fit (See Sec.3.1 for further details). While the line features are analyzed separately for each epoch.

2.2. RGS

We retrieve 15 epochs of RGS observations for Mrk 3. After checking the flaring particle background, 4 epochs with an all-time high background have been abandoned, leaving a total clean exposure of 130.8 ks as seen in Table 1. We extract the spectra from the two RGS modules

¹ <https://ned.ipac.caltech.edu>

Table 1. Log of X-ray observations

Inst	Obs ID	Start Date (UT)	Net Exposure (ks)
HETG	873	2000-03-18 06:58:08	100.6
HETG	12874	2011-04-19 15:53:47	77.06
HETG	12875	2011-04-25 09:34:32	29.86
HETG	13254	2011-08-26 02:56:58	31.53
HETG	13261	2011-05-02 00:17:30	22.08
HETG	13263	2011-04-28 23:08:33	19.72
HETG	13264	2011-04-27 19:45:10	35.76
HETG	13406	2011-05-03 12:54:21	21.43
HETG	14331	2011-08-28 13:09:38	51.21
RGS	0009220301	2001-03-12 23:10:35	4.2
RGS	0009220401	2002-03-10 13:17:59	16.9
RGS	0009220501	2002-03-25 17:05:48	13.6
RGS	0009220601	2001-03-20 20:03:15	22.5
RGS	0009220701	2001-03-28 20:47:56	6.9
RGS	0009220901	2001-09-12 00:27:09	5.1
RGS	0009221601	2002-09-16 05:09:12	4.5
RGS	0656580301	2012-03-15 11:27:22	40.8
RGS	0741050101	2015-03-19 17:32:26	4.0
RGS	0741050201	2015-04-08 16:23:36	5.8
RGS	0741050401	2015-04-20 15:39:41	6.5

following the standard pipeline *rgsproc* with the SAS v21.0.0 software package (Gabriel et al. 2004). These spectra are divided into 3 groups according to observation start time (2001-2002, 2012, and 2015) and co-added respectively. We find very little spectral variability across epochs. Thus all the RGS spectra are co-added together.

3. RESULTS

Spectra have been optimally rebinned and analyzed with SPEX v 3.08.01 (Kaastra et al. 2024). Galactic foreground absorption with column density $N_{\text{H,gal}} = 9.28 \times 10^{22}$ has always been included during spectral modeling by introducing a *hot* model with temperature fixed at 92.8 K. Error bars of the derived properties are taken as the 1- σ (68.3%) confidence level, unless otherwise mentioned in the following sections.

3.1. Modeling Baseline Continuum

Co-added HEG spectrum of Mrk 3 over the 2 – 10 keV band consists of an intrinsically absorbed power law with a distinct absorption edge around 7 keV, a prominent fluorescent Fe K α line and a reflection component. We

adopt a photoionized absorber (*pion*(abs)_{torus}) in front of the baseline power-law (*pow*) to account for the intrinsic absorption. Especially, PION can simultaneously calculate and fit the illuminating continuum and ionization balance in a self-consistent way. A reflection component (*refl*) has also been added to describe the baseline continuum. The absorption edge energy ($\simeq 7.11$ keV in the source frame) indicates that the intrinsic absorber is almost neutral. Allowing the ionization parameter (ξ) of *pion*_{torus} to vary freely during the fitting causes it to peg at the lower limit. So we fix ξ of this component to the 3- σ upper limit of -2 . Testing values lower than -2 , results in negligible differences to the best fit. The best-fit column density of this neutral absorber is $1.73^{+0.14}_{-0.13} \times 10^{24}$ cm $^{-2}$ and it could be associated with the torus around AGN. Other best-fit parameters have been recorded in the column HEG_{con} of Table 2.

Our result is roughly consistent with previous studies, indicating that the intrinsic torus column density in Mrk 3 lies near the boundary between the Compton-thin and Compton-thick regimes. Yaqoob et al. (2015) and Guainazzi et al. (2016) adopt self-consistent torus model with careful analysis, and conclude that the central AGN should be classified as Compton-thin. It should be noted that there are slight discrepancies between our derived torus parameters and previous studies. The main reason is that, the reflection model we applied in *SPEX* is built for plane-parallel, Compton-thick scattering material. Our baseline model is therefore not fully self-consistent in this context, but it provides a reasonable approximation. So we adopt it in the following analysis for simplification.

We also divide spectra of all the epochs into 2 groups depending on the observation time (epoch 2000 and 2011). The X-ray continuum below 10 keV is relatively stable as can be seen from Fig. 2.

3.2. redshifted Ionized Absorber

Two residual absorption line features can be found around 6.5–6.8 keV in the co-added HEG spectrum. The centroids of these two absorption lines are 6.60 ± 0.04 keV and 6.82 ± 0.03 keV if fitted with two gaussian models. They could be assigned to He-like (6.70 keV) and H-like (6.97 keV) Fe K α lines with consistent redshifted velocity of around $\sim 4 \times 10^3$ km s $^{-1}$.

3.2.1. Inflowing Absorber Inside the Torus

The two absorption-line features are present in both 2000 and 2011 observations (See Fig. 2). The persistent existence spanning 11 years suggests that it may not be transient. Thus we add an additional redshifted absorber *pion*(abs)_{red} to account for this highly ionized

inflowing absorption component and place it inside the neutral torus absorber, closer to the central black hole.

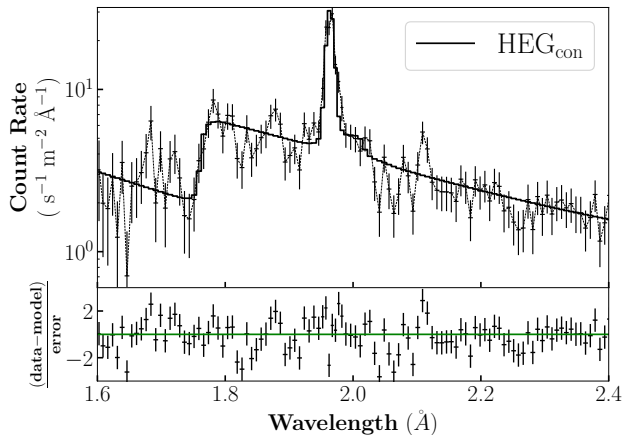


Figure 1. Co-added HEG spectra of Mrk 3. Black solid line represents the best-fit continuum model, involving a power-law continuum, a reflection component and neutral absorption from torus. Residual absorption line features remain around 1.85 – 1.95 Å.

We noticed prominent variability of the redshifted absorption features across epochs, which must be taken into account. Phenomenological Gaussian modeling indicates that the centroids of the two highly ionized Fe absorption lines consistently shift by $\Delta v \sim 3 \times 10^3$ km s⁻¹ from 2000 to 2011, suggesting a potential deceleration of the ionized absorber between the two epochs. To derive the properties of this redshifted absorber, we fit the spectra of the two epochs separately with an additional redshifted PION(abs)_{red}. The best-fit results are summarized in the columns of HEG₂₀₀₀ and HEG₂₀₁₁ of Table 2.

In this scenario, both the photon index of the illuminating power-law and the column density of torus for the two epochs are roughly consistent with the baseline fitting of co-added spectrum (HEG_{con}) in Sec. 3.1. However, the reflection fraction (~ 0.07 and ~ 0.031) becomes smaller. This reduction is due to the presence of the additional redshifted absorber model, which attenuates the incident continuum and leads to a higher best-fit normalization of the unabsorbed power-law component I_{PL} . The actual absolute magnitude of the reflection component I_{refl} remains unchanged. As a result the reflection fraction $scal = \frac{I_{refl}}{I_{PL}}$ decreases.

Over the 11 years, the velocity of the putative inflowing absorber decelerates from $6.1 \pm 0.5 \times 10^3$ km s⁻¹ to $3.4 \pm 0.3 \times 10^3$ km s⁻¹. Its velocity broadening σ_v also slightly decreases from $\sim 8 \times 10^2$ km s⁻¹ to $\sim 2.7 \times 10^3$ km s⁻¹, with large uncertainties. Both the

column density and ionization parameter increase with the decreasing of the bulk velocity across epochs.

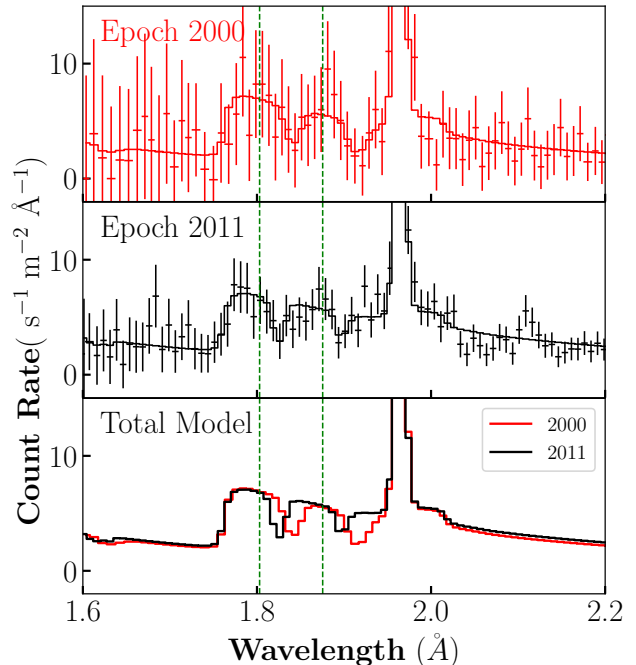


Figure 2. *The top and middle panel:* HEG spectra of Mrk 3 for epoch 2000 (red) and epoch 2011 (black). A redshifted photoionized absorber has been added to the baseline continuum model. Crosses mark the observation data and solid lines represent the best-fit model. Green dashed vertical lines indicate the rest-frame centroids for H-like (1.779 Å) and He-like (1.851 Å) iron lines in Mrk 3. These absorption features are persistent over a time interval spanning over 11 yrs, while the inflowing velocity slightly decelerates from $6.1 \pm 0.5 \times 10^3$ km s⁻¹ to $3.4 \pm 0.3 \times 10^3$ km s⁻¹. The column density and ionization parameter increase over the time. *The bottom panel:* Comparison of the best-fit total models between epoch 2000 (red line) and epoch 2011 (black line). Clear shifts of absorption line centroids are present across epochs.

3.2.2. Alternative geometry

We also examined an alternative geometry, placing the redshifted absorber outside the torus. However, this configuration fails to produce a good fit, as most of the high energy photons are already absorbed by the inner torus and cannot further ionize Fe ions to the observed high states.

Another possible scenario is that the highly ionized absorber is not inside the torus and photoionized by the central AGN, but instead represents hot, dense collisionally ionized gas in the host galaxy that is moving

Table 2. Best-fit results for HEG spectral modeling

Mod	Par	Unit	HEG _{con}	HEG ₂₀₀₀	HEG ₂₀₁₁	HEG _{alter}
epoch			co-added	2000	2011	co-added
band		Å	1.6 – 6.2	1.6 – 6.2	1.6 – 6.2	1.6 – 6.2
pow	Γ	-	2.24 ± 0.06	$2.07^{+0.07}_{-0.08}$	$2.32^{+0.05}_{-0.06}$	2.25 ± 0.06
	Norm	$10^{52} \text{ ph s}^{-1} \text{ keV}^{-1}$	8^{+3}_{-2}	16^{+19}_{-8}	60^{+25}_{-17}	10^{+4}_{-3}
refl	scal	-	$0.20^{+0.07}_{-0.05}$	$0.07^{+0.07}_{-0.04}$	$0.031^{+0.011}_{-0.009}$	$0.026^{+0.005}_{-0.005}$
pion(abs)_{torus}	$\log(\xi)$	$\log(\text{erg cm s}^{-1})$	-2	-2	-2	-2
	N_{H}	10^{24} cm^{-2}	$1.73^{+0.14}_{-0.13}$	$2.1^{+0.4}_{-0.3}$	$1.82^{+0.16}_{-0.14}$	$1.85^{+0.15}_{-0.13}$
pion(abs)_{red}	$\log(\xi)$	$\log(\text{erg cm s}^{-1})$	-	$3.5^{+0.6}_{-0.2}$	$4.5^{+0.4}_{-0.3}$	-
	N_{H}	10^{24} cm^{-2}	-	$0.26^{+1.01}_{-0.13}$	$2.0^{+2.1}_{-1.8}$	-
	v_{bulk}	10^3 km s^{-1}	-	$+6.1 \pm 0.5$	3.4 ± 0.3	-
	σ_v	km s^{-1}	-	$8^{+5}_{-4} \times 10^2$	$2.7^{+1.3}_{-1.1} \times 10^2$	-
hot(abs)_{red}	T	keV	-	-	-	15^{+9}_{-4}
	N_{H}	10^{24} cm^{-2}	-	-	-	2.79 ± 0.07
	v_{bulk}	10^3 km s^{-1}	-	-	-	$3.3^{+0.3}_{-0.2}$
C -stat			849.32	663.39	777.94	832.37
d.o.f			612	590	607	609

away from us along line of sight. Based on the base-line continuum model in Sec. 3.1, a collisionally ionized absorber model **hot(abs)_{red}** is placed outside the torus to fit the co-added HEG spectrum, as shown in the column HEG_{alter} in Table 2. This model gives a best-fit with C -stat (832.4 for 609 d.o.f). The temperature of the putative hot gas reaches 15^{+9}_{-4} keV. The presence of such hot and fast moving gas is difficult to explain by any mechanism unrelated to the central AGN.

3.3. Modeling the Soft X-ray Band

Multiple emission lines are clearly present in the co-added RGS spectrum. Instead of phenomenological gaussian models, we adopt physical emission models of collisionally ionized/photoionized gas embedded in SPEX (CIE/PION) rather than using phenomenological Gaussian lines. We adopt a similar underlying base-line continuum model as described in Section 3.1, consisting of an incident power-law continuum absorbed by the AGN torus. The reflection component is negligible in the soft X-ray band, and after evaluation we ignore it for simplification. The ionization parameter ξ and column density N_{H} of the torus are fixed at the values derived from co-added HEG spectrum.

First, we try to reproduce the multiple lines with emission from a single static photoionized gas component (**pion(emis)₁**). We denote this model set as RGS_{PI}. Gas in the vicinity of the black hole can naturally be illuminated and ionized by the central AGN. We assume that the power-law continuum irradiating the static pho-

toionized gas is identical to that irradiating the torus. The covering factor omeg of **pion(emis)₁** is fixed at unity for simplicity. The best-fit column density N_{H} is $2.9 \pm 0.3 \times 10^{21} \text{ cm}^{-2}$. Detailed fitting results can be refer to Table 3 and Figure 3. The best-fit model underestimates the emission lines around 8.5 Å, 12.5 Å and 17.2 Å.

Adding a second photoionized emission component (**pion(emis)₂**) improves the fit with a C -stat reduction of in 119.5 for 5 extra degrees of freedom (d.o.f). Detailed best-fit parameters of this new model set are listed in the column RGS_{PI+PI} in Table 3. The illuminating power-law continuum and the bulk motion velocity of this new **pion(emis)₂** are allowed to vary, representing a potential (narrow-line region) outflow responding to a different illuminating continuum to the static photoionized gas. And the best-fit Γ for the outflowing photoionized gas is 1.26 ± 0.06 , roughly consistent with the fiducial model set RGS_{PI+PI}. This model slightly overpredicts the continuum level at short wavelength $\lesssim 7.5$ Å. Both the static and outflowing photoionized gas metallicity are assumed to be solar abundance. We test allowing the iron abundance to vary freely, but the best-fit abundance still remains around 1. A more flexible model is examined, in which the illuminating power law for the torus, the staic, and the outflowing photoionized components are all allowed to vary. However, the fit cannot converge successfully probably restricted by the spectral quality. We have also tried an alternative assumption

that the torus and the outflowing $\text{pion}(\text{emis})_2$ share the same illuminating power law. This results in a slightly worse C -stat of 571.

We attempt to substitute the outflowing photoionized component $\text{pion}(\text{emis})_2$ with a collisionally ionized component in solar metallicity. The best-fit result is recorded in the column $\text{RGS}_{\text{PI+CI}}$ of the Table 3 and Figure 3. The temperature of the cie gas is 0.96 ± 0.02 keV and it is outflowing with a blueshifted velocity of ~ 740 km s^{-1} . Compared to $\text{RGS}_{\text{PI+PI}}$, this model reduces C -stat for 12 with one fewer free parameter, implying a better fit. To further assess the goodness of fit, we calculate the corrected Akaike Information Criterion ($cAIC = -2\ln L + 2k + \frac{2k^2+2k}{n-k-1}$) (Akaike 1974; Franklin et al. 2002; Liddle 2007), where k represents the number of free model parameters and n denotes the number of spectral bins. The likelihood L between the model m_i and data d_i is described by $L = \prod_i \frac{\exp(-m_i)m_i^{d_i}}{d_i!}$ for C -stat. The $cAIC$ does not require the model to be nested, making it particularly suitable for evaluating alternative physical scenarios. The $cAIC$ for $\text{RGS}_{\text{PI+CI}}$ (321.0) reduces for 7 compared to $\text{RGS}_{\text{PI+PI}}$ (328.0). This corresponds to a confidence level of $\sim 97\%$ that $\text{RGS}_{\text{PI+CI}}$ is favored.

There remain some discrepancies between model and observation around Si XIII and Fe XXII lines, probably due to enhancement in element abundance. We allow the iron abundance of the outflowing CIE gas to vary freely. A new best-fit summarized in Table 3 with the column of $\text{RGS}_{\text{PI+CI,sub } Z_{\odot}}$ has been achieved, with a sub-solar iron abundance $Z_{\text{Fe}} = 0.22 \pm 0.03 Z_{\odot}$. The $cAIC$ for $\text{RGS}_{\text{PI+CI,sub } Z_{\odot}}$ (313.6) further reduces 7.4 for one extra free parameter compared to the result with solar metallicity.

Adding further one more photoionized or collisional ionized component does not improve the goodness of fitting and thus is not necessary. So we conclude that the PI+CI with sub-solar metallicity scenario is preferred.

4. DISCUSSION

4.1. Inflowing torus clumps

A redshifted, highly ionized absorber at a high velocity of several 10^3 km s^{-1} has been detected from the HEG spectrum, persistent over a timescale of at least 11 yrs. The most probable explanation for this inflowing while decelerating highly ionized absorber is that, instability at the outer surface of the torus leads to the evaporation of the torus clumps. These clumps are stretched and drawn inward toward the accretion flow under the

gravitational influence of the central SMBH, and subsequently become highly ionized under the intense radiation field, as schematically illustrated in Figure 4. This process is expected to occur stochastically and persistently. The observed H-like and He-like iron absorption lines thus trace the extended inflowing material that connects between the clumpy torus and accretion disk.

Assuming that the thickness of this absorber is comparable to its distance from the ionizing source (i.e., $\Delta r = r \lesssim \frac{L_{\text{ion}}}{N_{\text{H}}\xi}$), we can estimate its number density and (maximum) radial location for 2000 and 2011 epochs, following standard practice in previous warm absorber studies (Krolik & Kriss 2001; Laha et al. 2016; Wang et al. 2022). The ionization luminosity of Mrk 3 over 13.6 eV – 13.6 keV is given by our best-fit model. The redshifted absorber is located at a distance of $r_{\text{max}} \lesssim 0.74$ pc ($\sim 3.4 \times 10^4 r_{\text{g}}$) since 2000, and reduces to $\lesssim 0.04$ pc ($\sim 1.8 \times 10^3 r_{\text{g}}$) in 2011, consistent with the observed increase in ionization parameter over time. As the absorber approaches the central black hole, its number density increases by nearly two orders of magnitude, while the line-of-sight velocity drops for $\sim 2.7 \times 10^3$ km s^{-1} . The derived properties of the infalling ionized absorber at both epochs are recorded in Table 4.

The redshifted absorption features exist in two epochs spanning 11 yrs. By multiplying this timescale with the inflowing velocity, we estimate the dynamical length (or depth) of the absorber along line-of-sight to be $r_{\text{dyn}} \sim 0.04 - 0.07$ pc. This value is comparable to the inferred r_{max} in 2011, lending support to our previous assumption that $\Delta r = r$.

The dust sublimation radius of Mrk 3 is estimated to be $R_{\text{sub}} = 0.5 L_{46}^{0.5} (\frac{1800}{T_{\text{sub}}})^{2.6} f(\theta) \sim 0.13$ pc, where L_{46} is AGN bolometric luminosity in units of 10^{46} erg s^{-1} (Barvainis 1987). For simplification, the dust sublimation temperature T_{sub} is chosen to be 1800 K and the angular-dependent geometrical factor is fixed at 1. This suggests the detected inflowing ionized absorber lies at a distance either interior to or comparable with the dusty torus of Mrk 3, consistent with our spectral modeling assumption that the inflowing absorber resides closer to the SMBH than the torus.

Guainazzi et al. (2016) reported a variability of 5 – 10% in the line-of-sight column density (N_{H}) within 3 – 30 d based on SED fitting of Mrk 3 NuSTAR spectra. These occultation events were interpreted as transits of small cloudlets within the torus, providing strong support for the clumpy nature of Mrk 3 torus. Notably, the best-fit column density of the highly-ionized redshifted absorber ($N_{\text{H,red}}$) in our analysis is of the same

Table 3. Best-fit results for RGS spectral modeling

Mod	Par	Unit	RGS _{PI}	RGS _{PI+CI}	RGS _{PI+PI}	RGS _{PI+CI,sub} Z_{\odot}
band		Å	6.2 – 24.8	6.2 – 24.8	6.2 – 24.8	6.2 – 24.8
pow	Γ	-	$1.006^{+0.009}_{-0.014}$	2.1 ± 0.5	2.4 ± 0.4	$2.9^{+0.5}_{-0.7}$
	Norm	10^{50} ph s ⁻¹ keV ⁻¹	6.1 ± 0.4	$4.8^{+1.1}_{-0.9}$	$4.7^{+1.0}_{-0.8}$	$2.7^{+0.9}_{-0.8}$
pion(abs) _{torus}	$\log(\xi)$	log(erg cm s ⁻¹)	-2	-2	-2	-2
	N_{H}	10^{24} cm ⁻²	1.85	1.85	1.85	1.85
pion(emis) ₁	$\log(\xi)$	log(erg cm s ⁻¹)	1.48 ± 0.02	$0.97^{+0.36}_{-0.06}$	$0.99^{+0.35}_{-0.17}$	$1.3^{+0.7}_{-0.5}$
	N_{H}	10^{21} cm ⁻²	2.9 ± 0.3	$2.7^{+0.8}_{-0.6}$	2.9 ± 0.3	$3.6^{+1.9}_{-1.0}$
cie	T	keV	-	0.96 ± 0.02	-	0.86 ± 0.03
	v_{bulk}	10^2 km s ⁻¹	-	$7.4^{+0.5}_{-0.9}$	-	3.3 ± 0.6
	Z_{Fe}	Z_{\odot}	-	1	-	0.22 ± 0.03
	Norm	10^{64} cm ⁻³	-	1.20 ± 0.05	-	2.56 ± 0.17
pion(emis) ₂	$\log(\xi)$	log(erg cm s ⁻¹)	-	-	2.10 ± 0.02	-
	N_{H}	10^{21} cm ⁻²	-	-	$0.404^{+0.026}_{-0.008}$	-
	v_{bulk}	10^2 km s ⁻¹	-	-	$6.7^{+0.9}_{-0.8}$	-
	Γ_{incident}		-	-	1.11 ± 0.02	-
C -stat			699.41	568.01	579.86	485.35
d.o.f			304	301	299	300

Table 4. Properties of the infalling absorber

Epoch	L_{ion}	r_{max}	n_{H}	$M_{\text{abs}}/C_{\text{f,abs}}$
	10^{45} erg s ⁻¹	pc	cm ⁻³	M_{\odot}
2000	1.9	0.74	1.1×10^5	4.7×10^4
2011	8.6	0.04	1.5×10^7	1×10^3

order of magnitude ($\sim 10^{24}$ cm⁻²) as that of the neutral torus ($N_{\text{H,torus}}$). Furthermore, the characteristic number density of individual torus clumps would be $\sim 10^5 - 10^7$ cm⁻³ (Netzer 2013), comparable to the estimated average density we infer for the infalling absorber ($\bar{n}_{\text{H,red}} \sim 10^6$ cm⁻³). These consistencies add weight to our aforementioned scenario in which the redshifted absorber originates from torus clumps.

We compare the total mass $M = \mu m_{\text{p}} n_{\text{H}} \frac{4}{3} \pi (R_{\text{out}}^3 - R_{\text{in}}^3) * C_{\text{f}}$ of the observed infalling absorber M_{abs} with that of the AGN torus M_{torus} . C_{f} can be interpreted as a combination of sky coverage ($\frac{\Omega}{4\pi}$) and volume filling factor inside the absorber. For M_{abs} , we take $R_{\text{in}} = r_{\text{max}}$ and assume $\Delta r = r$. The total mass of the infalling ionized absorber decreases from $M_{\text{abs,2000}} \sim 4.7 \times 10^4 M_{\odot} * C_{\text{f,abs}}$ in epoch 2000 to $M_{\text{abs,2011}} \sim 1 \times 10^3 M_{\odot} * C_{\text{f,abs}}$ in epoch 2011, recorded in Table 4. For the AGN torus, we adopt a characteristic

number density ($n_{\text{H,torus}} \sim 10^{4-5}$ cm⁻³) and the best-fit average column density $N_{\text{H,torus}} \sim 2 \times 10^{24}$ cm⁻² from our spectral modeling. The inner radius of the torus $R_{\text{in,torus}}$ is assumed to correspond to the dust sublimation radius $R_{\text{sub}} \sim 0.13$ pc. The total mass of AGN torus is estimated to be $M_{\text{torus}} \sim 5 \times 10^{(5-7)} M_{\odot} * C_{\text{f,torus}}$. While the covering factors, $C_{\text{f,abs}}$ and $C_{\text{f,torus}}$ are hard to constrain, it is reasonable to assume that the torus has larger or comparable covering factor as the redshifted absorber. So the estimated torus mass is of several orders of magnitude larger than the ionized absorber, consistent with our scenario that the infalling absorber originates from the torus.

4.2. Deceleration mechanism

The deceleration of the ionized absorber suggests the presence of an extra force acting against the gravitational pull of the central SMBH. The observed deceleration rate is $a_{\text{obs}} \sim -0.73$ cm s⁻² with the negative sign denoting force direction away from SMBH). The outward radiative acceleration exerted on the redshifted absorber ($a_{\text{rad}} \equiv \frac{F_{\text{abs}}}{\mu m_{\text{p}} N_{\text{H}} c} \sim 7 \times 10^{-15}$ cm s⁻²) is significantly smaller than the inward gravitational acceleration $a_{\text{grav}} \equiv \sim 0.95$ cm s⁻². F_{abs} represents the absorbed flux and we take the solar proton-to-electron abundance $\mu = 1.4$. The radiation pressure is insufficient to compete with gravity, likely because the observed ionized absorber is too close to the central illuminating source and is already heavily ionized.

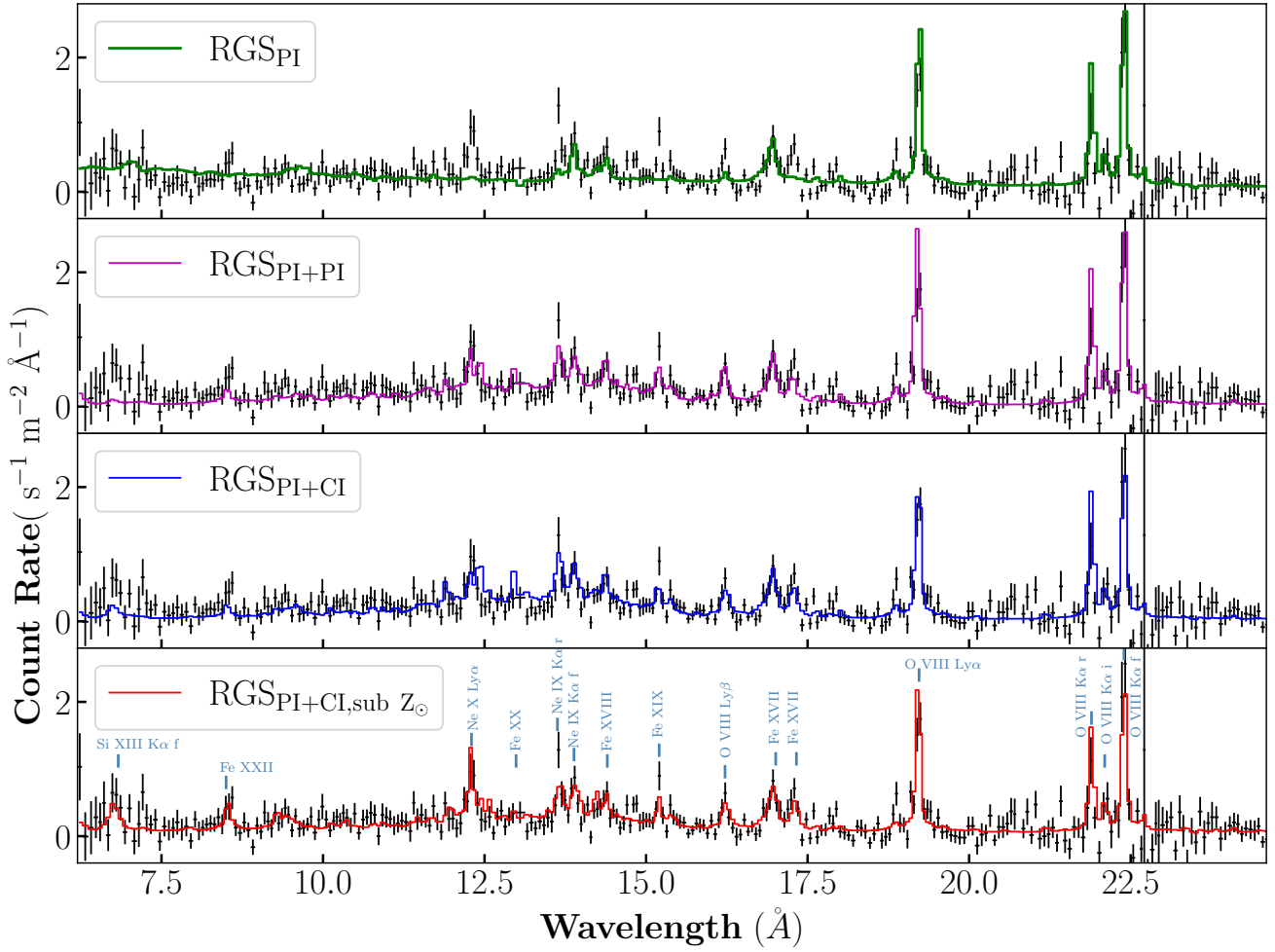


Figure 3. Spectral modeling of co-added RGS spectrum for Mrk3 over 6.2 – 24.8 Å. Black crosses mark the observed data and error. Solid lines represent the best-fit models. The baseline continuum consists of an incident power-law, a reflection component and torus absorption fixed at the best-fit value from co-added HEG spectrum. *The first panel:* Spectrum fitted with one single photoionized emission gas component ($\text{pion}(\text{emis})_1$) in addition to the baseline. Clear residual lines remain around 8.5 Å, 12.5 Å and 17.2 Å. *The second panel:* Adding the second photoionized gas component ($\text{pion}(\text{emis})_2$) would overestimate the continuum level of short wavelength $\lesssim 10$ Å. *The third panel:* Substituting the second $\text{pion}(\text{emis})_2$ with a collisionally ionized gas component (cie) in solar metallicity. *The forth panel:* The most preferred model consists of a static photoionized gas and an outflowing collisionally ionized gas with sub-solar iron abundance $\sim 0.22 Z_\odot$. The temperature of the gas is ~ 1 keV and the blueshifted velocity is ~ 740 km s^{-1} .

One possible explanation for the deceleration is ram pressure exerted by a putative disk wind. Highly ionized, high-velocity outflows are prevalent in luminous AGN. Ultra-fast outflows (UFOs), characterized by blueshifted K-shell absorption lines of H-like and He-like Fe with velocity exceeding 10^4 km s^{-1} can be found in up to 40% in local Seyfert galaxies (Tombesi & Cappi 2014). The deceleration exerted on the inflowing absorber by such a ‘putative’ wind can be estimated as $a_{\text{wind}} = -\frac{\rho(v_{\text{wind}} + v_{\text{abs}})^2 S_{\text{abs}}}{M_{\text{abs}}}$, where S_{abs} stands for the cross-sectional area of between inflowing absorber and the wind. We also assume the covering factor of the inflowing absorber is equivalent to its sky coverage $C_{f,\text{abs}} = \frac{\Omega}{4\pi} = \frac{S_{\text{abs}}}{4\pi r_{\text{max}}^2}$ and r_{max} is the derived

location of the absorber. Thus the ram pressure deceleration from the putative wind can be expressed as $a_{\text{wind}} = -\mu m_{\text{p}} n_{\text{wind}} (v_{\text{wind}} + v_{\text{abs}})^2 4\pi r_{\text{max}}^2 \frac{C_{f,\text{abs}}}{M_{\text{abs}}}$. Here the relative speed between the putative wind and inflowing absorber $v_{\text{wind}} + v_{\text{abs}}$ is considered. n_{wind} represents the number density of the putative wind. Based on the total mass $\frac{M_{\text{abs}}}{C_{f,\text{abs}}}$ and the location r_{max} of the absorber estimated from Table 4, a UFO with a typical number density n_{wind} around $\sim (2 - 4) \times 10^6$ cm^{-3} and a velocity of $\sim 10^4$ km s^{-1} can provide a deceleration rate $a_{\text{ram}} \sim -3.7 - -0.5$ cm s^{-2} , comparable to the observed value. However, such a disk wind is elusive to detection, probably due to the narrow opening angle of such UFO

and the misalignment between its outflow direction and our line of sight toward Mrk 3.

We have also considered the ram pressure braking by the dense broad line region (BLR) clouds. Similarly, the deceleration caused by the ambient, nearly static BLR clouds can be expressed as $a_{\text{BLR}} = -\mu m_{\text{p}} n_{\text{BLR}} v_{\text{abs}}^2 4\pi r_{\text{max}}^2 \frac{C_{\text{f,abs}}}{M_{\text{abs}}}$. Here v_{abs} describes the relative speed between the inflowing absorber and the dense BLR clouds. Assuming a typical average density for the BLR clouds $n_{\text{BLR}} \sim 10^8 \text{ cm}^{-3}$, the deceleration rate is estimated to be $-2.6 - -61 \text{ cm s}^{-2}$, which is also sufficient, possibly even excessive, to brake the fast-infalling material. Given the clumpy nature of BLR gas, such braking effect may not occur continuously. We speculate that the BLR cloud is also a plausible candidate to cause the observed deceleration.

4.3. Kinematics of the inflowing absorber

We compare the mass inflow rate of the detected ionized absorber with the intrinsic accretion rate of Mrk 3. The mass inflow rate of the redshifted ionized absorber is estimated as $\dot{M}_{\text{in,WA}} = 4\pi\mu m_{\text{p}} n_{\text{H}} v_{\text{in}} r_{\text{max}}^2 \times C_{\text{f}} \sim (36 - 163 M_{\odot} \text{ yr}^{-1}) \times C_{\text{f}}$. Homogeneous absorber is assumed for simplification and a correction factor C_{f} is included. For Mrk 3, the unabsorbed 2 – 10 keV luminosity from our best-fit model is $L_{2-10} = 5.1 \times 10^{44} \text{ erg s}^{-1}$, corresponding to a bolometric luminosity of $L_{\text{bol}} \sim 5.1 \times 10^{45} \text{ erg s}^{-1}$ after applying a bolometric correction factor 10 (Duras et al. 2020). Assuming a $\eta = 10\%$ energy transfer efficiency, the mass accretion rate at the event horizon is $\dot{M}_{\text{in,EH}} \equiv \frac{L_{\text{bol}}}{\eta c^2} \sim 0.9 M_{\odot} \text{ yr}^{-1}$.

The inflow rate of the ionized absorber is almost 50 times higher than the mass accretion rate at the event horizon. These infalling torus clumps are sufficient to supply the accretion and maintain the nuclear activity in Mrk 3, provided that the correction factor $C_{\text{f}} \gtrsim 0.03$. Probably these evaporated torus clumps possess a small sky covering factor and form stream-like structures above the torus surface, continuously fueling the accretion of central AGN. This may also explain the rarity of redshifted absorber detections, which requires a grazing line of sight to torus. Alternatively, and more likely, only $\sim (0.6 - 3)\%$ of the inflowing material finally reaches the accretion disk, with the majority being entrained and ejected by a putative disk wind. The derived n_{H} and N_{H} of the infalling ionized absorber increase during its deceleration, while its velocity dispersion σ_v decreases, implying that the velocity gradient is being suppressed. These observational signatures further supports the scenario that the ionized absorber is compressed and becomes denser as it approaches the SMBH.

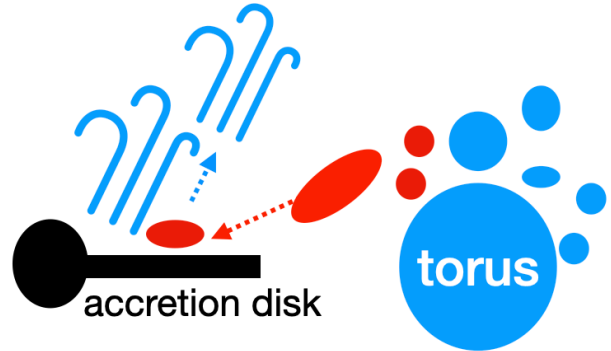


Figure 4. A diagram for the sub-parsec scale gas environment around Mrk 3. Some torus clumps are evaporated and fall toward the central black hole, serving as a disk-feeding inflow. The inflowing ionized absorber would be decelerated or even ejected by a putative disk wind.

4.4. Shocked interstellar medium in the NLR

The soft X-ray emission of Mrk 3 can be described by one photoionized plasma component together with one outflowing collisionally ionized plasma component.

The photoionized component is likely associated with emission from the narrow-line region and is nearly static, with a 3σ upper limit of $\lesssim 173 \text{ km s}^{-1}$ for outflow velocity. In the optical band, three photoionized gas components have been adopted to describe emission lines detected by Hubble *STIS* in the NLR of Mrk 3 (Collins et al. 2005, 2009). We find that the ionization parameter of our soft X-ray photoionized plasma ($\log(U) \sim -0.8$) is even higher than that of the most highly ionized optical components ($\log(U) \sim -1.5$), suggesting that the soft X-ray trace emission from the inner part of NLR, close to the central AGN. Considering a typical gas density of NLR to be $\sim 10^3 - 10^5 \text{ cm}^{-3}$, the soft X-ray emission is estimated to come from gas around 0.8 – 8 pc, based on the best-fit ionization parameter $\xi = \frac{L_{\text{ion}}}{n_e r^2}$.

The collisionally ionized plasma component, with a blueshifted velocity of $\sim 740 \text{ km s}^{-1}$, could trace the shocked interstellar medium (ISM) as proposed by (Bogdán et al. 2017). Our best-fit gas temperature ($\sim 0.86 \text{ keV}$) and iron abundance ($\sim 0.22 Z_{\odot}$) are consistent with those derived from their MEG observation ($\sim 0.85 \text{ keV}$ and $Z = 0.24$). They also suggest that the shocked gas component extends toward east and west, in alignment with the extended biconical warm ionized gas outflows traced by optical emission lines (e.g., [O III] and $\text{H}\alpha$). The average velocity of the [O III] outflow is $\sim 500 \text{ km s}^{-1}$, spanning over 10 – 300 pc (Ruiz et al. 2001; Gnilka et al. 2020; Meena et al. 2023), in agreement with the blueshifted velocity of the collisionally ionized soft X-ray gas. The outflow rate of [O III] gas

peaks at $\sim 8 M_{\odot} \text{ yr}^{-1}$ around 200 pc from the SMBH (Revalski et al. 2021), indicating that the biconical NLR outflow may be generated or accelerated at larger distances. A putative disk wind could propagate outward, interact with the surrounding medium, shock and excite the NLR outflow.

4.5. Coherent scenario

Overall, we propose a coherent scenario in Mrk 3 as illustrated by Figure 4. The redshifted, highly-ionized absorber observed in the hard X-ray band traces the inflowing clumps originated from torus instability. These clumps are evaporated from the torus at sub-parsec scales and serve as potential fuel for black hole accretion, falling roughly along the opening angle of the torus surface. Mrk 3, with a grazing line-of-sight configuration, may represent a local analog to the small sample of $z \sim 1$ quasars, where parsec-scale inflows connecting torus and disk are characterized by broad/narrow optical absorption lines (Zhou et al. 2019; Chen et al. 2022). The deceleration of the inflowing ionized absorber indirectly supports the existence of a putative disk wind. Such a disk wind could also entrain and eject the accretion material away, explaining the reason why only a small fraction of the inflowing material finally reaches the black hole event horizon. The disk wind can propagate outward and interact with the surrounding ISM, traced by shocked collisionally ionized ~ 1 keV gas in soft X-ray band. It is also a promising candidate for driving or accelerating the biconical [O III] outflows in the NLR up to hundred-parsec scale. However, there are no clear spectral signatures of such a disk wind, probably because the opening angle of the wind is narrow and its outflow direction is out of our sight line.

5. SUMMARY

We analyze the high resolution X-ray spectroscopic data of Mrk 3 nuclei and provide the direct evidence of sub-parsec scale feeding inflows bridging the gap between torus and SMBH accretion disk. Our main results are as follows:

- A fast inflowing, highly ionized absorber characterized by redshifted Fe XXV and Fe XXVI absorption lines has been detected in the Chandra HEG spectra. It decelerates from $6.1 \pm 0.5 \times 10^3 \text{ km s}^{-1}$ to $3.4 \pm 0.3 \times 10^3 \text{ km s}^{-1}$ over 11 years. Photoionization modeling suggests that both the ionization parameter and column density increase during the deceleration, accompanied with a decrease in the distance to central black hole from $\lesssim 0.74 \text{ pc}$ to $\lesssim 0.04 \text{ pc}$.

- The inflowing ionized absorber is estimated to be located between the outer accretion disk and torus, with a mass inflow rate of $\sim (36 - 163) \times C_f M_{\odot} \text{ yr}^{-1}$. Compared with the accretion rate of Mrk 3, only $\sim (0.6 - 3)\%$ of the inflowing material finally reaches the event horizon.
- Multiple emission lines detected in soft X-ray band can be well described by an almost static gas component illuminated by the central AGN, together with a collisionally ionized gas component with temperature of $0.86 \pm 0.03 \text{ keV}$ and sub solar metallicity ($Z_{\text{Fe}} \sim 0.22 Z_{\odot}$) outflowing at a velocity of $\sim 330 \text{ km s}^{-1}$.
- We propose a probable scenario to explain the gas dynamics in sub-parsec scale in Mrk 3. Torus clumps are evaporated and fall toward central black hole due to instability, manifesting as redshifted ionized absorber in a grazing line of sight to torus. The inflowing material is decelerated by the ram pressure from either dense BLR cloud or a putative ultra-fast disk wind. Such a disk wind lacks direct detection but is supported by the existence of a soft X-ray outflowing gas and the biconical [O III] outflow in the NLR of Mrk 3.

AGN with such grazing-view in the local Universe like Mrk 3 would enable us to pierce into the fueling inflow connecting torus and outer accretion disk. With high-resolution X-ray spectroscopy like Chandra HETG and XRISM Resolve, we would expect to find more cases with similar orientation. A comprehensive study of both inflow and outflow down to sub-parsec scale near the central engine is vital to obtain a clear insight of the feedback effect connecting multi-scale, multi-phase gas environment around SMBH.

We thank Junjie Mao, Daniele Rogantini, Mengfei Zhang, Yulong Gao, Suoqing Ji, Feng Yuan and Zhiyuan Li for helpful discussions and critical comments. We would like to acknowledge the organizing committee of the *I-HOW COSPAR Workshop 2024: A New Era of High-Resolution X-ray Spectroscopy* who inspired the basic idea and provided a platform for collaboration of this work. F.S. is supported in part by the China Postdoctoral Science Foundation (grants 2022TQ0354 and 2022M723279). Y.J.W. acknowledges support by National Natural Science Foundation of China (Project No. 12403019) and Jiangsu Natural Science Foundation (Project No. BK20241188).

Facilities: CXO, XMM-Newton

Software: CIAO(Fruscione et al. 2006), SAS(Gabriel et al. 2004), SPEX(Kaastra et al. 2024), PION(Mehdipour et al. 2016)

REFERENCES

- Akaike, H. 1974, IEEE Transactions on Automatic Control, 19, 716
- Barvainis, R. 1987, ApJ, 320, 537, doi: [10.1086/165571](https://doi.org/10.1086/165571)
- Bogdán, Á., Kraft, R. P., Evans, D. A., Andrade-Santos, F., & Forman, W. R. 2017, ApJ, 848, 61, doi: [10.3847/1538-4357/aa8c76](https://doi.org/10.3847/1538-4357/aa8c76)
- Chen, Z.-F., Gu, M., He, Z., et al. 2022, A&A, 659, A103, doi: [10.1051/0004-6361/202142307](https://doi.org/10.1051/0004-6361/202142307)
- Collins, N. R., Kraemer, S. B., Crenshaw, D. M., Bruhweiler, F. C., & Meléndez, M. 2009, ApJ, 694, 765, doi: [10.1088/0004-637X/694/2/765](https://doi.org/10.1088/0004-637X/694/2/765)
- Collins, N. R., Kraemer, S. B., Crenshaw, D. M., et al. 2005, ApJ, 619, 116, doi: [10.1086/426314](https://doi.org/10.1086/426314)
- Crenshaw, D. M., & Kraemer, S. B. 2012, ApJ, 753, 75, doi: [10.1088/0004-637X/753/1/75](https://doi.org/10.1088/0004-637X/753/1/75)
- Duras, F., Bongiorno, A., Ricci, F., et al. 2020, A&A, 636, A73, doi: [10.1051/0004-6361/201936817](https://doi.org/10.1051/0004-6361/201936817)
- Fabian, A. C. 2012, ARA&A, 50, 455, doi: [10.1146/annurev-astro-081811-125521](https://doi.org/10.1146/annurev-astro-081811-125521)
- Franklin, A. B., Anderson, D. R., & Burnham, K. P. 2002, Journal of Applied Statistics, 29, 267, doi: [10.1080/02664760120108719](https://doi.org/10.1080/02664760120108719)
- Fruscione, A., McDowell, J. C., Allen, G. E., et al. 2006, in Society of Photo-Optical Instrumentation Engineers (SPIE) Conference Series, Vol. 6270, Observatory Operations: Strategies, Processes, and Systems, ed. D. R. Silva & R. E. Doxsey, 62701V, doi: [10.1117/12.671760](https://doi.org/10.1117/12.671760)
- Gabriel, C., Denby, M., Fyfe, D. J., et al. 2004, in Astronomical Society of the Pacific Conference Series, Vol. 314, Astronomical Data Analysis Software and Systems (ADASS) XIII, ed. F. Ochsenbein, M. G. Allen, & D. Egret, 759
- Gnilka, C. L., Crenshaw, D. M., Fischer, T. C., et al. 2020, ApJ, 893, 80, doi: [10.3847/1538-4357/ab8000](https://doi.org/10.3847/1538-4357/ab8000)
- Guainazzi, M., Risaliti, G., Awaki, H., et al. 2016, MNRAS, 460, 1954, doi: [10.1093/mnras/stw1033](https://doi.org/10.1093/mnras/stw1033)
- Izumi, T., Wada, K., Imanishi, M., et al. 2023, Science, 382, 554, doi: [10.1126/science.adf0569](https://doi.org/10.1126/science.adf0569)
- Kaastra, J. S., Raassen, A. J. J., de Plaa, J., & Gu, L. 2024, SPEX X-ray spectral fitting package, 3.08.01, Zenodo, doi: [10.5281/zenodo.12771915](https://doi.org/10.5281/zenodo.12771915)
- Krolik, J. H., & Kriss, G. A. 2001, ApJ, 561, 684, doi: [10.1086/323442](https://doi.org/10.1086/323442)
- Laha, S., Guainazzi, M., Chakravorty, S., Dewangan, G. C., & Kembhavi, A. K. 2016, MNRAS, 457, 3896, doi: [10.1093/mnras/stw211](https://doi.org/10.1093/mnras/stw211)
- Liddle, A. R. 2007, MNRAS, 377, L74, doi: [10.1111/j.1745-3933.2007.00306.x](https://doi.org/10.1111/j.1745-3933.2007.00306.x)
- Meena, B., Crenshaw, D. M., Schmitt, H. R., et al. 2023, ApJ, 943, 98, doi: [10.3847/1538-4357/aca75f](https://doi.org/10.3847/1538-4357/aca75f)
- Mehdipour, M., Kaastra, J. S., & Kallman, T. 2016, A&A, 596, A65, doi: [10.1051/0004-6361/201628721](https://doi.org/10.1051/0004-6361/201628721)
- Netzer, H. 2013, The Physics and Evolution of Active Galactic Nuclei (Cambridge University Press)
- Revalski, M., Meena, B., Martinez, F., et al. 2021, ApJ, 910, 139, doi: [10.3847/1538-4357/abdca4](https://doi.org/10.3847/1538-4357/abdca4)
- Ruiz, J. R., Crenshaw, D. M., Kraemer, S. B., et al. 2001, AJ, 122, 2961, doi: [10.1086/323917](https://doi.org/10.1086/323917)
- Shi, X.-H., Jiang, P., Wang, H.-Y., et al. 2016, ApJ, 829, 96, doi: [10.3847/0004-637X/829/2/96](https://doi.org/10.3847/0004-637X/829/2/96)
- Storchi-Bergmann, T., & Schnorr-Müller, A. 2019, Nature Astronomy, 3, 48, doi: [10.1038/s41550-018-0611-0](https://doi.org/10.1038/s41550-018-0611-0)
- Tombesi, F., & Cappi, M. 2014, MNRAS, 443, L104, doi: [10.1093/mnrasl/slu091](https://doi.org/10.1093/mnrasl/slu091)
- Tombesi, F., Cappi, M., Reeves, J. N., et al. 2010, A&A, 521, A57, doi: [10.1051/0004-6361/200913440](https://doi.org/10.1051/0004-6361/200913440)
- Wang, Y., Kaastra, J., Mehdipour, M., et al. 2022, A&A, 657, A77, doi: [10.1051/0004-6361/202141599](https://doi.org/10.1051/0004-6361/202141599)
- Woo, J.-H., & Urry, C. M. 2002, ApJ, 579, 530, doi: [10.1086/342878](https://doi.org/10.1086/342878)
- Yaqoob, T., Tatum, M. M., Scholtes, A., Gottlieb, A., & Turner, T. J. 2015, MNRAS, 454, 973, doi: [10.1093/mnras/stv2021](https://doi.org/10.1093/mnras/stv2021)
- Zhou, H., Shi, X., Yuan, W., et al. 2019, Nature, 573, 83, doi: [10.1038/s41586-019-1510-y](https://doi.org/10.1038/s41586-019-1510-y)